Quantum metasurfaces of arrays of Λ-emitters for photonic nano-devices

Ryzhov, Igor V.; Malikov, Ramil F.; Malyshev, Andrey V.; Malyshev, Victor A.

Published in:
Journal of Optics (United Kingdom)

DOI:
10.1088/2040-8986/ac2788

Publication date:
2021

PAPER

Quantum metasurfaces of arrays of Λ-emitters for photonic nano-devices

IOP Publishing Journal of Optics
J. Opt. **23** (2021) 115102 (14pp) https://doi.org/10.1088/2040-8986/ac2788

Quantum metasurfaces of arrays of Λ-emitters for photonic nano-devices

Igor V Ryzhov[1], Ramil F Malikov[2], Andrey V Malyshev[3,4,*] and Victor A Malyshev[1,5]

[1] Herzen State Pedagogical University, 191186 St. Petersburg, Russia
[2] M. Akmullah Bashkir State Pedagogical University, 450008 Ufa, Russia
[3] GISC, Departamento de Física de Materiales, Universidad Complutense, E-28040 Madrid, Spain
[4] Ioffe Physical-Technical Institute, 26 Politechnicheskaya Street, 194021 St. Petersburg, Russia
[5] Zernike Institute for Advanced Materials, University of Groningen, Nijenborgh 4, 9747 AG Groningen, The Netherlands

E-mail: a.malyshev@fis.ucm.es

Received 16 August 2021, revised 14 September 2021
Accepted for publication 16 September 2021
Published 20 October 2021

Abstract

We address exotic optical response of a planar metasurface comprising a monolayer of regularly spaced quantum three-level emitters with a doublet in the ground state (the so-called Λ-emitters). All emitters are coupled by the retarded dipole field which depends on the current state of all emitters. This coupling introduces a feedback into the system. Complex interplay of the latter with the intrinsic nonlinearity of a three-level system results in several remarkable effects in the monolayer's optical response, such as multistability, self-oscillations, and chaos. The peculiarity of the considered system is that some of the predicted nonlinear effects manifest themselves at very low excitation field intensities (on the order of 1 W/cm^2), which is advantageous for possible applications: the monolayer can operate as a perfect reflector, a bistable mirror, and a THz or noise generator. It is argued therefore that the proposed system is a promising candidate for a building block for various photonic nano-devices.

Keywords: optics of metamaterials, optical nonlinear dynamics, optical instabilities and complexity

(Some figures may appear in colour only in the online journal)

1. Introduction

After the discovery of graphene [1, 2] other crystalline (quasi)two-dimensional (2D) materials with fascinating optical and transport properties have been fabricated, such as transition metal dichalcogenides [3–6] hexagonal boron nitride, black phosphorous, and other inorganic quasi-2D systems (see for reviews [7–10]), as well as mixed-dimensional van der Waals heterostructures [11], artificial 2D supercrystals based on semiconductor quantum dots (SQDs) [12–14], organic 2D polymers [15], and 2D nanostructures assembled from sequence-defined molecules (DNAs, peptides etc) [16].

Assemblies of SQDs organized periodically are of special interest from the viewpoint of optical and opto-electronic applications because they can absorb light over the whole optical spectrum, from the infrared to the ultraviolet. Compared to an isolated SQD, heterostructures provide additional degrees of freedom for controlling their properties, such as lattice geometry and material parameters, which opens unprecedented possibilities to engineer optical properties of these systems opening promising perspectives for nanophotonics. One of the key ingredients of dense 2D optical systems is the long range interaction between emitters; it results in many promising effects (see for example [17–19] and references therein). In particular, the band structure [20–24] and linear optical properties [25, 26] of 2D supercrystals have been also addressed recently, showing that the lattice geometry alone provides considerable room for tuning of the physical properties of these structures. Nonlinear optical response of these systems is a more intriguing and challenging problem and has not been widely discussed so far.

In recent publications, [27–29] the nonlinear optical response of a 2D supercrystal comprising SQDs with a

* Author to whom any correspondence should be addressed.

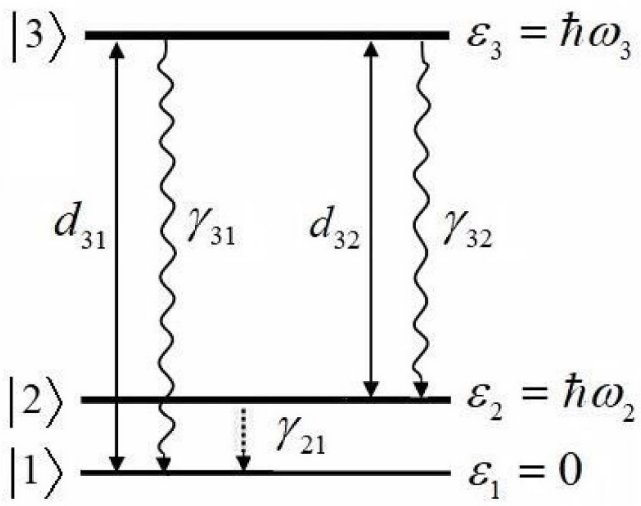

Figure 1. Energy level diagram of a Λ-emitter comprising the upper state $|3\rangle$ and the lower doublet states $|2\rangle$ and $|1\rangle$. The energies of these states are $\varepsilon_3 = \hbar\omega_3$, $\varepsilon_2 = \hbar\omega_2$, and $\varepsilon_1 = \hbar\omega_1 = 0$. Solid arrows indicate the optically allowed transitions with corresponding transition dipole moments $\mathbf{d}_{32}$ and $\mathbf{d}_{31}$. Wavy arrows denote the spontaneous decay of the upper state to the states of the doublet with rates γ_{32} and γ_{31}. Dashed arrow indicates the relaxation within the doublet with rate γ_{21}.

ladder arrangement of the energy levels has been investigated theoretically. It has been found that this system can manifest fascinating nonlinear optical effects, including multistability, periodic and aperiodic self-oscillations, chaos, and transient chaos. 2D arrays of V-type quantum emitters reveal similar features [30–33]. The underlying characteristic that gives rise to these nonlinear effects is the secondary field produced by the optical transition dipoles, which introduces a mirrorless feedback into the system. The interplay of the latter with the intrinsic nonlinearity of emitters themselves gives rise to the above mentioned exotic optical response of the SQD supercrystals.

In this paper, we investigate theoretically the nonlinear optical response of a monolayer of Λ-emitters, i.e. three-level systems with a single upper state and a doublet in the ground state (see figure 1 for the level schematics). Doped quantum dots [34] and organic nanocrystals with vibronic structure of the ground state [35] are some examples of such type of emitters. Due to high density of emitters and high oscillator strengths of the optical transitions, the total (retarded) dipole-dipole interactions among emitters have to be taken into account. The real part of this interaction results in the dynamic shift of the emitter's energy levels while the imaginary part describes the collective radiative decay of emitters; both parts depend on the population differences among levels (see, e.g. [36, 37]). These two effects are crucial for the nonlinear dynamics of the system. As a result, in addition to bistability, analogous to that manifested by a thin layer of two-level emitters, [36–44] we predict multistability, self-oscillations and chaotic behavior in the optical response of the supercrystal of Λ-emitters. Within a certain spectral range, the monolayer operates as a bistable mirror, similar to a 2D supercrystal of SQDs with the ladder and V arrangement of the energy levels [27–29, 32]. To uncover the character of the instabilities, we use the standard methods of nonlinear dynamics, such as the analysis of the Lyapunov exponents, bifurcation diagrams, phase-space maps, and Fourier spectra [45–53]. To the best of our knowledge, a detailed study of the optical response of assemblies of Λ-emitters has not been carried out so far (some preliminary results have been reported in a short paper [54]).

The paper is organized as follows. In the next section, we describe the model of a monolayer comprising Λ-emitters and the mathematical formalism that we use to study it. The formalism is based on the density matrix approach to the description of the optical dynamics of an isolated emitter combined with the equation for the field acting on it; the latter is addressed within the mean-field approximation. In section 3, we present the results of numerical calculations of the monolayer optical response, including the stationary solution (section 3.1), analysis of bifurcations (section 3.2), and the system dynamics (section 3.3). Discussion of the underlying physical mechanisms of the predicted effects is provided in section 3.4. In section 4, the close-to-unity reflectance of the monolayer is discussed. We conclude and argue about the relevance of our results for practical applications in section 5.

2. Model and theoretical background

We address a 2D $N \times N$ square lattice of quantum emitters spaced by the lattice constant a. All emitters comprising the monolayer have the Λ-type arrangement of the energy levels (as shown in figure 1) in which transitions are allowed only between the upper state $|3\rangle$ and either the doublet $|1\rangle$ or $|2\rangle$ states. These transitions are characterized by the transition dipole moments $\mathbf{d}_{31}$ and $\mathbf{d}_{32}$, respectively. For the sake of simplicity, we set them to be real and parallel to each other and to one of the lattice vectors, so that $\mathbf{d}_{32} = \mu\mathbf{d}_{31} \equiv \mu\mathbf{d}$. The upper state $|3\rangle$ can decay spontaneously to the states of the doublet $|2\rangle$ and $|1\rangle$ with the rates γ_{32} and γ_{31}, respectively, which obey the relationship $\gamma_{32} = \mu^2\gamma_{31}$. The doublet splitting ω_{21} is assumed to be small compared to the optical transition frequencies $\omega_{32} = \omega_3 - \omega_2$ and $\omega_{31} = \omega_3 - \omega_1$. We consider also the normal incidence of the external field polarized along the transition dipole moments (which is not an essential restriction[6]) and having the frequency ω_0.

The optical dynamics of the monolayer is governed by the Lindblad quantum master equation for the density operator $\rho(t)$ [55, 56]. Within the mean-field and the rotating wave approximations this equation reads

$$\dot{\rho}(t) = -\frac{i}{\hbar}\left[H^{\mathrm{RWA}}(t), \rho(t)\right] + \mathcal{L}\{\rho(t)\}, \tag{1a}$$

$$H^{\mathrm{RWA}}(t) = \hbar\left(\Delta_{21}\sigma_{22} + \Delta_{31}\sigma_{33}\right) - i\hbar\left[\Omega_{31}(t)\sigma_{31} + \Omega_{32}(t)\sigma_{32}\right] + h.c., \tag{1b}$$

[6] Considerations of other polarizations of the incident field would introduce an unnecessary technical complications while it can be taken into account by rescaling the incident intensity.

$$\mathcal{L}\{\rho(t)\} = \frac{1}{2}\gamma_{31}\left([\sigma_{13}\rho(t),\sigma_{31}] + [\sigma_{13},\rho(t)\,\sigma_{31}]\right) + \frac{1}{2}\gamma_{32}\left([\sigma_{23}\rho(t),\sigma_{32}] + [\sigma_{23},\rho(t)\,\sigma_{32}]\right) + \frac{1}{2}\gamma_{21}\left([\sigma_{12}\rho(t),\sigma_{21}] + [\sigma_{12},\rho(t)\,\sigma_{21}]\right), \quad (1c)$$

$$\sigma_{ij} = |i\rangle\langle j|, \quad i,j = 1,2,3, \quad (1d)$$

where the dot in equation (1*a*) denotes the time derivative, $\hbar$ is the reduced Plank constant, H^{RWA} is the Λ-emitter Hamiltonian in the rotating wave approximation (RWA), square brackets denote commutators, $\mathcal{L}$ is the Lindblad relaxation operator given by equation (1*c*) [55, 56]. In equation (1*b*), $\hbar\Delta_{21} = \hbar(\omega_2 - \omega_1)$ is the doublet energy splitting, while $\hbar\Delta_{31} = \hbar(\omega_3 - \omega_0)$ is the energy of the state $|3\rangle$ in the rotating frame. Alternatively, the quantity Δ_{31} can be interpreted as the detuning of the incident field frequency ω_0 from the resonance frequency of the $1 \leftrightarrow 3$ transition. Likewise, $\Delta_{32} = \Delta_{31} - \Delta_{21}$ is the detuning from the frequency of the $2 \leftrightarrow 3$ transition. We define also $\Omega_{31}(t) = \mathbf{d}_{31}\cdot\mathbf{E}(t)/\hbar \equiv \Omega(t)$ and $\Omega_{32}(t) = \mathbf{d}_{32}\cdot\mathbf{E}(t)/\hbar \equiv \mu\Omega(t)$, where $\mathbf{E}(t)$ is the slowly-varying amplitude of the total mean field acting on a Λ-emitter. The latter field is the sum of the amplitude of the incident field, $\mathbf{E}_0(t)$, and the amplitude of the secondary field produced by all others dipoles at the position of the given Λ-emitter. Thus, $\Omega(t)$ is the Rabi amplitude of the mean field and can be written in the following form [29] (hereafter, we omit the explicit time dependence in all variables)

$$\Omega = \Omega_0 + (\gamma_{\mathrm{R}} - i\Delta_{\mathrm{L}})(\rho_{31} + \mu\rho_{32}), \quad (2)$$

where $\Omega_0 = \mathbf{d}_{31}\cdot\mathbf{E}_0/\hbar$ is the Rabi amplitude of the incident field and the second term represents the Rabi amplitude of the secondary field, in which the two terms proportional to γ_{R} and Δ_{L} are far-zone and near-zone fields, respectively. The near-zone field is analogous to the Lorentz local-field correction [57]. In the general case, γ_{R} and Δ_{L} depend on the lattice geometry and the ratio of the reduced excitation wavelength $\lambda\!\!\!^{-} = \lambda/(2\pi)$ to the linear system size. For a simple square lattice of emitters with the linear size Na one obtains [29]

$$\gamma_{\mathrm{R}} = \frac{3}{8}\gamma_{31}N^2, \quad (3a)$$

$$\Delta_{\mathrm{L}} \approx 3.39\,\gamma_{31}\left(\frac{\lambda\!\!\!^{-}}{a}\right)^3, \quad (3b)$$

if Na$\ll \lambda\!\!\!^{-}$ (point-like system). In the opposite case of Na$\gg \lambda\!\!\!^{-}$ (extended system), γ_{R} and Δ_{L} are given by [29]

$$\gamma_{\mathrm{R}} \approx 4.51\,\gamma_{31}\left(\frac{\lambda\!\!\!^{-}}{a}\right)^2, \quad (4a)$$

$$\Delta_{\mathrm{L}} \approx 3.35\,\gamma_{31}\left(\frac{\lambda\!\!\!^{-}}{a}\right)^3. \quad (4b)$$

As follows from equations (3*a*) to (4*a*), γ_{R} is determined by either the total number of emitters in the system (for a point-like system: Na$\ll \lambda\!\!\!^{-}$) or by the number of emitters within the area of $\lambda\!\!\!^{-2}$ (for an extended sample: Na$\gg \lambda\!\!\!^{-}$). The physical meaning of the parameter γ_{R} is clear then: it is nothing but the Dicke superradiant constant [29, 58–60] which determines the collective radiation relaxation rate of Λ-emitters in the monolayer.

On the other hand, the parameter Δ_{L} is almost independent of the system size; [29] it describes the near-zone dipole-dipole interaction of a Λ-emitter with all others. The latter interaction is what introduces a strong feedback into the system; for realistic systems $\Delta_{\mathrm{L}} \gtrsim 1000\ \gamma_{31}$, giving rise to an additional strong nonlinearity. Also, for a dense extended sample ($\lambda\!\!\!^{-} \gg a$), which is the most interesting case we address hereafter: $\Delta_{\mathrm{L}} \gg \gamma_{\mathrm{R}}$.

In the basis of the states $|1\rangle$, $|2\rangle$, and $|3\rangle$, the system of equations equations (1*a*)–(1*c*) for the density matrix elements $\rho_{\alpha\beta}$ ($\alpha,\beta = 1,2,3$) of a Λ-emitter in the monolayer reads

$$\dot{\rho}_{11} = \gamma_{21}\rho_{22} + \gamma_{31}\rho_{33} + \Omega^*\rho_{31} + \Omega\rho_{31}^*, \quad (5a)$$

$$\dot{\rho}_{22} = -\gamma_{21}\rho_{22} + \gamma_{32}\rho_{33} + \mu(\Omega^*\rho_{32} + \Omega\rho_{32}^*), \quad (5b)$$

$$\dot{\rho}_{33} = -(\gamma_{31} + \gamma_{32})\rho_{33} - \Omega^*\rho_{31} - \Omega\rho_{31}^* - \mu(\Omega^*\rho_{32} + \Omega\rho_{32}^*), \quad (5c)$$

$$\dot{\rho}_{31} = -\left[i\Delta_{31} + \frac{1}{2}(\gamma_{31} + \gamma_{32})\right]\rho_{31} + \Omega(\rho_{33} - \rho_{11}) - \mu\Omega\rho_{21}, \quad (5d)$$

$$\dot{\rho}_{32} = -\left[i\Delta_{32} + \frac{1}{2}(\gamma_{31} + \gamma_{32} + \gamma_{21})\right]\rho_{32} + \mu\Omega(\rho_{33} - \rho_{22}) - \Omega\rho_{21}^*, \quad (5e)$$

$$\dot{\rho}_{21} = -\left(i\Delta_{21} + \frac{1}{2}\gamma_{21}\right)\rho_{21} + \mu\Omega^*\rho_{31} + \Omega\rho_{32}^*. \quad (5f)$$

Equations (5*a*)–(5*f*) conserve the total population, $\rho_{11} + \rho_{22} + \rho_{33} = 1$, i.e. we consider the spontaneous decay to be the only channel of the population relaxation. Dephasing of the Λ-emitter states is also neglected, which is a reasonable assumption for the cryogenic temperatures.

3. Numerical results

In our numerical calculations we used the following set of parameters (similar to those in [29]): $\gamma_{31} \approx 3\times10^9\ \mathrm{s}^{-1}$, the ratio $\mu = d_{32}/d_{31} = (\gamma_{32}/\gamma_{31})^{1/2}$ is taken to be unity for simplicity. The magnitudes of γ_{R} and Δ_{L} depend on the ratio $\lambda\!\!\!^{-}/a$. Taking $\lambda\!\!\!^{-} \sim 100 \div 200$ nm and $a \sim 10 \div 20$ nm, we obtain the following estimates: $\gamma_{\mathrm{R}} \sim 10^{12}\ \mathrm{s}^{-1}$ and $\Delta_{\mathrm{L}} \sim 10^{13}\ \mathrm{s}^{-1}$.

Accordingly, we set $\gamma_R = 100\gamma_{31}$ and $\Delta_L = 1000\gamma_{31}$. In what follows, the spontaneous emission rate γ_{31} is used as the unit of all quantities having dimension of frequency, while ${\gamma_{31}}^{-1}$ is used as the time unit.

The remaining two parameters are the doublet splitting Δ_{21} and the relaxation rate γ_{21} in the $2 \to 1$ channel. As we show below, the optical response of the system is very sensitive to these two parameters which can be tuned in an experiment, for example, by the magnetic field or the temperature, for which reason they are considered to be variable quantities. We note that in the case of the ladder-like arrangement of the energy levels (see for example, [29]), there are no analogs of the low-frequency coherence ρ_{21} and its adjustable relaxation described by the rate γ_{21}, making the Λ-type system qualitatively different from the ladder-like one. The $2 \to 1$ relaxation channel provides an additional tunable degree of freedom that can be used to tailor the optical response of the monolayer of Λ-emitters.

First, we address the optical response for the case in which the incident field is in resonance with the transition $1 \leftrightarrow 3$ of an *isolated* Λ-emitter, i.e. $\Delta_{31} = 0$, $\Delta_{32} = -\Delta_{21}$. Here, it is important to point out that the bare resonances, $\Delta_{31} = 0$ and $\Delta_{32} = 0$, are renormalized (dressed) by the secondary field which acts on the emitter. Apart from shifting the energy levels the secondary field couples the two transitions, $1 \leftrightarrow 3$ and $2 \leftrightarrow 3$. As the result, one of these dressed resonances remains approximately unchanged $\tilde{\Delta}_{31} \approx \Delta_{31} = 0$, while the other shifts down to $\tilde{\Delta}_{31} \approx \Delta_L$ (see section 3.4 for more detailed discussion). The monolayer optical response in the vicinity of $\Delta_{31} = \Delta_L$ will be considered as well (section 4).

The system of equations (5*a*)–(5*f*) is a system of stiff differential equations, characterized by several significantly different time scales. In our case, they are $\gamma_{31}^{-1} \gg \gamma_R^{-1} \gg \Delta_L^{-1}$. The doublet splitting Δ_{21} and the relaxation rate γ_{21} bring in two additional time scales. To solve the system numerically we use specialised routines for stiff systems.

3.1. Stationary analysis

In this section we consider the stationary regime, setting to zero all time derivatives in equations (5*a*)–(5*f*). To solve these stationary equations, we use the new analytical method developed in the recent paper, [29]. The results calculated for two values of the doublet splitting Δ_{21} and two relaxation rates γ_{21} are presented in figure 2.

As is seen from figure 2, the Rabi magnitude $|\Omega|$ of the mean field can have several solutions (up to five for $\gamma_{21} = 0.05$ and $\Delta_{21} = 15$) for some values of the Rabi magnitude $|\Omega_0|$ of the incident field. To explore the stability of different solutions, we used the standard Lyapunov exponents analysis [48, 49] calculating the eigenvalues Λ_k ($k = 1, 2, \ldots, 8$) of the Jacobian matrix of the right hand side of equations (5*a*)–(5*f*) as a function of $|\Omega|$. The Lyapunov exponent with the maximal real part determines the character of a stationary solution: if $\max_k\{\mathrm{Re}\,[\Lambda_k]\} \leqslant 0$ the solution is stable and unstable otherwise. The values of $\max_k\{\mathrm{Re}\,[\Lambda_k]\}$ are plotted in the right part of each panel in figure 2.

Note a very important feature of the stationary characteristics: not only branches with the negative slope are unstable, which is always the case, but also some parts of branches with the positive slopes. Quite remarkably, both the lower and upper stationary branches are only partially stable. In particular, for $\Delta_{21} = 100$, the stationary curve is unstable within a wide range of Rabi magnitudes $|\Omega_0|$.

3.2. Bifurcation diagrams

The bifurcation diagram is a powerful tool to explore possible scenarios of a dynamical system behavior [47, 48, 50, 53]. The diagram represents the system dynamics qualitatively as a function of some controlling (bifurcation) parameter. In our case, the most natural bifurcation parameter is the Rabi magnitude $|\Omega_0|$ of the incident field, while the Rabi magnitude of the mean field $|\Omega|$ is one of the possible measurable outputs. Below, we describe briefly an efficient procedure of constructing the bifurcation diagram, which was proposed in [29].

For each value of $|\Omega_0|$ and appropriate sets of initial conditions, equations (5*a*)–(5*f*) are integrated until all transients vanish and the system reaches an attractor. Then all the extrema of $|\Omega(t)|$ on the attractor are obtained over a sufficiently long time interval T. All the extremal values of $|\Omega(t)|$ are then plotted as points for the current value of the Rabi magnitude $|\Omega_0|$. The set of such points plotted for all values of $|\Omega_0|$ form the bifurcation diagram. The distribution of the extrema of $|\Omega(t)|$ provides qualitative information on possible types of the system dynamics. For example, if the dynamics converges to a stable fixed point, all the extrema collapse onto a single point given by the corresponding stable stationary solution. If the system is on a periodic orbit, all the extrema collapse onto a finite set of points separated by gaps. Quasiperiodic motion would appear as vertical bars separated by gaps, while chaos would manifest itself as a continuous vertical line. For more detail, see [29].

Figures 3 and 4 show the bifurcation diagrams, calculated as described above, for the case when the incident field is tuned to the resonance $1 \leftrightarrow 3$ of the isolated Λ-emitter (i.e. $\Delta_{31} = 0, \Delta_{32} = -\Delta_{21}$). The data presented in figure 3 are obtained for the doublet splitting $\Delta_{21} = 15$, while those in figure 4—for $\Delta_{21} = 100$. The relaxation constant $\gamma_{21} = 0.01$ in both cases. The double-S-shaped stationary characteristics (solid black and dashed red curves), which are taken from figure 2, are also given for reference. Upper panels in both figures display the overall bifurcation diagram, while the lower ones show blow ups of regions with interesting bifurcations.

Trivial parts of the bifurcation diagrams coincide with the stable part of the corresponding stationary curves (stable fixed points). However, there are also parts of the bifurcation diagrams which reveal more interesting dynamics. For example, there are sets of thin lines of points separated by gaps corresponding to some periodic orbits or limit cycles (see the vicinity of $|\Omega_0| \approx 50$). There are also dense features formed by vertical very dense lines of points, suggesting that the extrema of the mean-field Rabi magnitude $|\Omega(t)|$ are distributed randomly, so that the signal can be of the chaotic nature. Thus, for different values of the Rabi magnitude $|\Omega_0|$ of the incident field,

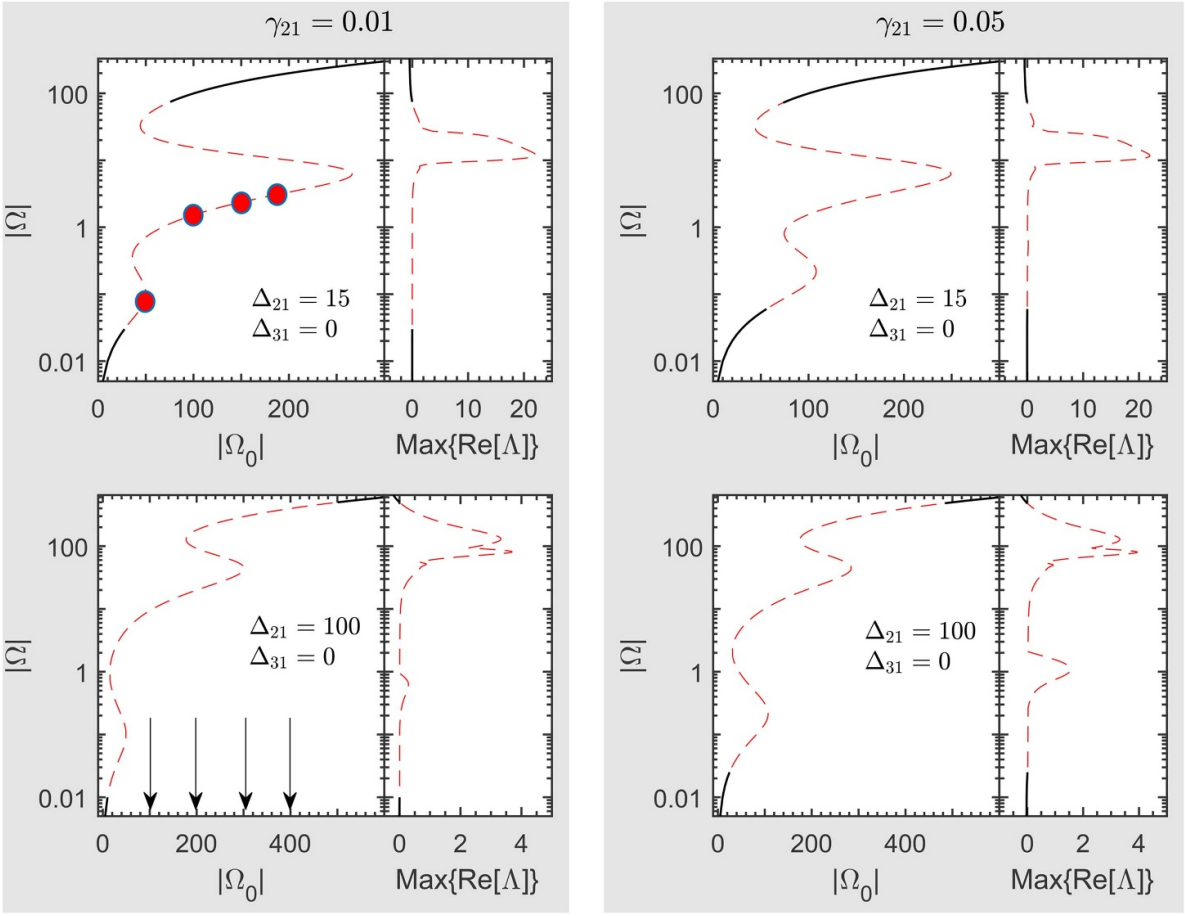

Figure 2. Stationary solutions to equations (2) and (5*a*)–(5*f*) obtained for the case when the incident field is in resonance with the transition $1 \leftrightarrow 3$ of an isolated Λ-emitter ($\Delta_{31} = 0$) for two values of the relaxation rate $\gamma_{21} = 0.01$ (left column) and $\gamma_{21} = 0.05$ (right column) and two values of the doublet splitting $\Delta_{21} = 15$ (upper row) and $\Delta_{21} = 100$ (lower row). Left panels in each plot present the stationary $|\Omega|$-vs-$|\Omega_0|$ dependence: stable (unstable) stationary solutions are shown by the solid black (dashed red) lines. Right-hand sides of the panels show the maximum value of the real parts of Lyapunov exponents. Filled circles in the upper left panel indicate the points that were further used as initial conditions for time-domain calculations of $|\Omega(t)|$ (see figure 5). Arrows in the lower left panel show the Rabi magnitudes $|\Omega_0|$, for which the time-domain behavior of $|\Omega(t)|$ was calculated for the ground state initial condition (see figure 6).

the system dynamics manifests various types of attractors. We address their properties in more details below (see section 3.3).

Figures 3 and 4 show that the system has different bifurcation points. Consider, for example, the vicinity of $|\Omega_0| \approx 15$ in the lower panel of figure 3; the system can only converge to the lower stable branch of the steady state (a fixed point) given by the thick solid black line. If $|\Omega_0|$ is increased the system would follow the lower branch until the latter looses stability at $|\Omega_0| \approx 25$ (the line changes from solid black to dashed red). At this point the system switches abruptly to the stable limit cycle which is enclosing the steady state branch (the limit cycle is given by thin black lines). Such a scenario is known as a subcritical Andronov-Hopf bifurcation. Then, if the field magnitude $|\Omega_0|$ is swept back the system would remain at the stable limit cycle attractor until the latter disappears at the saddle-node bifurcation of limit cycles (limit cycle folding point) [47, 50, 53] at $|\Omega_0| \approx 19.3$. Note that the two bifurcations occur at different values of $|\Omega_0|$, so the bifurcation diagram manifests a typical hysteresis.

The next couple of bifurcations can be seen at about $|\Omega_0| \approx$ 120–130 in figure 3, where two limit cycles seem to get folded. Finally, at about $|\Omega_0| \approx 160$ (the left side of the dense feature) a limit cycle switches to a chaotic trajectory. From that moment on, if the field amplitude is increased slowly enough, the system remains on a chaotic trajectory until the latter disappears at about $|\Omega_0 \approx 210|$, and the system switches to a stable fixed point (the upper stable branch of the stationary solution). Note that upper stable branch coexists with other attractors within a wide range of the bifurcation parameter, which suggests that their basins of attraction are well separated.

As far as the chaotic trajectories in figure 3 are concerned, given that they coexist with fixed points, such a chaos can be of the transient nature. If the system is let to evolve for sufficiently long time, it might finally end up at the stable stationary point (a steady-state). However, the lifetime of a chaotic transient can be very long, and it is hardly predictable; this time is known to be very sensitive to initial conditions and even to the integration method, which is a typical feature of a transient

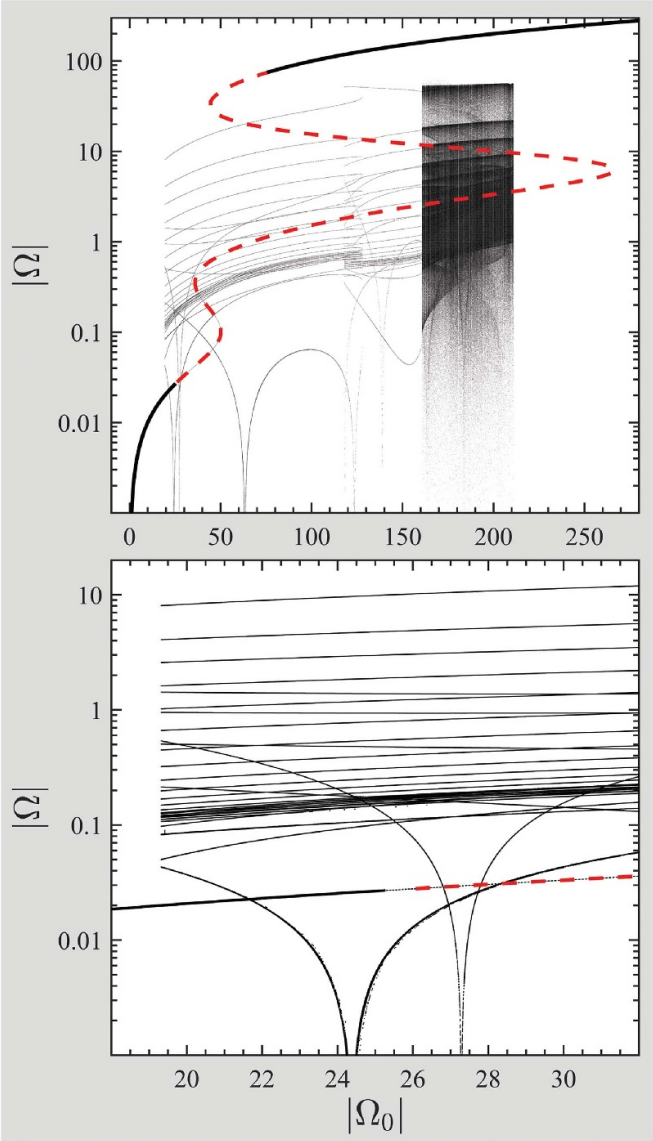

Figure 3. Top: the overall bifurcation diagram (extrema of the Rabi magnitude $|\Omega(t)|$ of the mean field as a function of the Rabi magnitude $|\Omega_0|$ of the incident field) calculated for the case when the incident field is in resonance with the transition $1 \leftrightarrow 3$ of an isolated Λ-emitter ($\Delta_{31} = 0$). Here, the doublet splitting $\Delta_{21} = 15$ and the relaxation rate $\gamma_{21} = 0.01$. The stationary (double S-shaped) solution is given for reference. Bottom: the blow-up of the part of the bifurcation diagram with nontrivial dynamics.

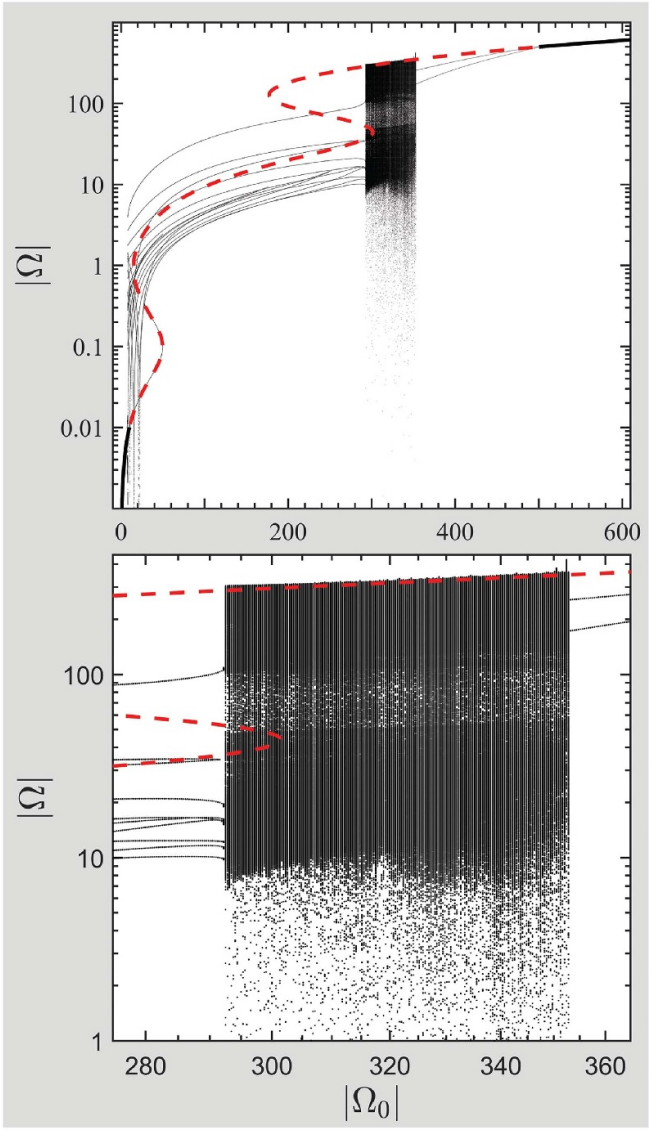

Figure 4. Same as in figure 3, but for $\Delta_{21} = 100$.

chaos (see [61, 62] and references therein). In our calculations, the system remained on the chaotic trajectory for the whole simulation time (over hundreds of orbits). We can therefore believe that it is an attractor. Nevertheless, we can not discard completely that it is a very long living transient in this case.

A very different scenario can be seen in the case of $\Delta_{21} = 100$ shown in figure 4. Here, there are bufurcations in which the limit cycle is converted into a chaotic trajectory and vice versa (see the vicinity of the dense feature blown up in the lower panel). In this case there are no coexisting stable fixed points, and the chaotic trajectories are real attractors. We have confirmed their chaotic nature by addressing their Fourier spectra and Lyapunov exponents (see the next section).

Finally, we would like to note that bifurcation diagrams of 2D systems of Λ-emitters are completely different from those of ladder-like systems [29], in particular, in the former case there are wide windows of parameters within which there are no stable solutions. Moreover, the instabilities are predicted here for very low intensities of the incident field (see also section 4), which is advantageous for experimental measurements and applications. A more detailed analysis of all possible bifurcations in the system is a stand-alone problem, which is beyond the scope of the present work.

3.3. Dynamics

In this section, we address a variety of nontrivial attractors. To do this, we solve equations (5*a*)–(5*f*) with two types of initial conditions: (a) the system is initially in the ground state (the only non-zero density matrix element is $\rho_{11}(0) = 1$), and

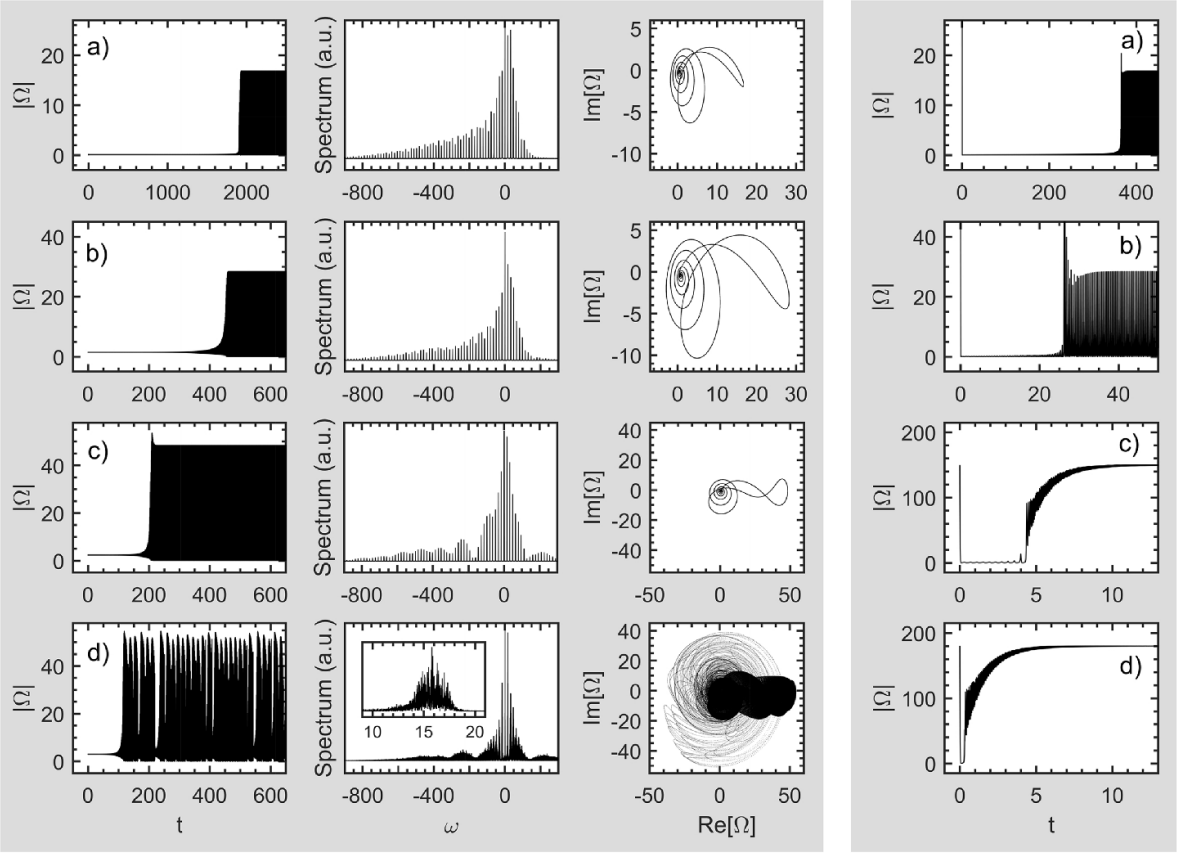

Figure 5. First column—time-domain behavior of the Rabi magnitude $|\Omega(t)|$ of the mean field, second column—the Fourier magnitude spectrum $\bar{f}(\omega)$, the third column—the two-dimensional phase-space map ($\mathrm{Re}\,\Omega$, $\mathrm{Im}\,\Omega$) of the attractor, calculated for the initial conditions that were the following points on the stationary characteristics: (a) $|\Omega_0| = 50$ and $|\Omega| = 0.0923$, (b) $|\Omega_0| = 100$ and $|\Omega| = 1.5213$, (c) $|\Omega_0| = 150$ and $|\Omega| = 2.3637$, (d) $|\Omega_0| = 180$ and $|\Omega| = 2.9251$. The inset shows the blow up of a quasi-continuous feature of the Fourier spectrum. Right column—time-domain behavior of the Rabi magnitude $|\Omega(t)|$ calculated for the ground state as the initial condition and at the same values of Rabi magnitude $|\Omega_0|$ of the incident field as in the left plot: (a) $|\Omega_0| = 50$, (b) $|\Omega_0| = 100$, (c) $|\Omega_0| = 150$, and (d) $|\Omega_0| = 180$. All quantities were calculated for the doublet splitting $\Delta_{21} = 15$ and the relaxation constant $\gamma_{21} = 0.01$.

(b) the system is initially in a stationary state. If the system was exactly in a stationary state it would remain there forever. However, due to the finite precision of calculations the system is always within a small vicinity of an exact stationary state. Therefore, it is either attracted to the stationary state if the latter is a steady-state, or drifts away from it otherwise.

The results of our numerical calculations are presented in figure 5 (for the doublet splitting $\Delta_{21} = 15$) and figure 6 (for $\Delta_{21} = 100$). The relaxation constant $\gamma_{21} = 0.01$ in both cases. Figure 5 shows the time-domain behavior of the mean-field magnitude $|\Omega(t)|$ in the first column, the Fourier magnitude spectra $\bar{f}(\omega) = |\int_T \Omega(t)\, e^{i\omega t} dt|$ in the second column, and the two-dimensional phase-space map ($\mathrm{Re}\,\Omega$, $\mathrm{Im}\,\Omega$) of the attractor in the third column. These results were calculated using the following stationary points (shown by filled circles in the upper panel of figure 2) as the initial conditions: (a) $|\Omega_0| = 50$ and $|\Omega| = 0.0923$, (b) $|\Omega_0| = 100$ and $|\Omega| = 1.5213$, (c) $|\Omega_0| = 150$ and $|\Omega| = 2.3637$, and (d) $|\Omega_0| = 180$ and $|\Omega| = 2.9251$. In the first three cases (a)–(c), the system evolves towards limit cycles, which is confirmed by the fact that the Fourier spectrum is a set of equidistant lines, while the trajectory in the phase space is apparently closed. Contrary to that, in the case (d) the attractor has characteristics typical for a chaotic motion: its Fourier spectrum is quasi-continuous, while the trajectory fills a finite area in the phase space. We have also calculated the Lyapunov exponents on the latter trajectory and found that one of them was positive, which confirms that the trajectory is chaotic.

The right column in figure 5 shows the time-domain behavior of the mean-field magnitude $|\Omega(t)|$ for the case when the system is initially in the ground state and for the same set of the incident field magnitudes $|\Omega_0|$: (a) $|\Omega_0| = 50$, (b) $|\Omega_0| = 100$, (c) $|\Omega_0| = 150$, and (d) $|\Omega_0| = 180$. In first two cases (panels (a) and (b)), the system evolves towards the limit cycles described by the Fourier spectrum and the phase map in rows two and three respectively. However, as it can be seen from the comparison of the dynamics presented in the first and the last columns (rows (a) and (b)), when the system starts from the ground state, it reaches the same limit cycle attractor much faster. On the other hand, in the last two cases (panels (c) and (d)) the system converges to fixed points on the upper stable branch of the stationary characteristics. Sensitivity to the initial conditions is an inherent property of dynamical systems

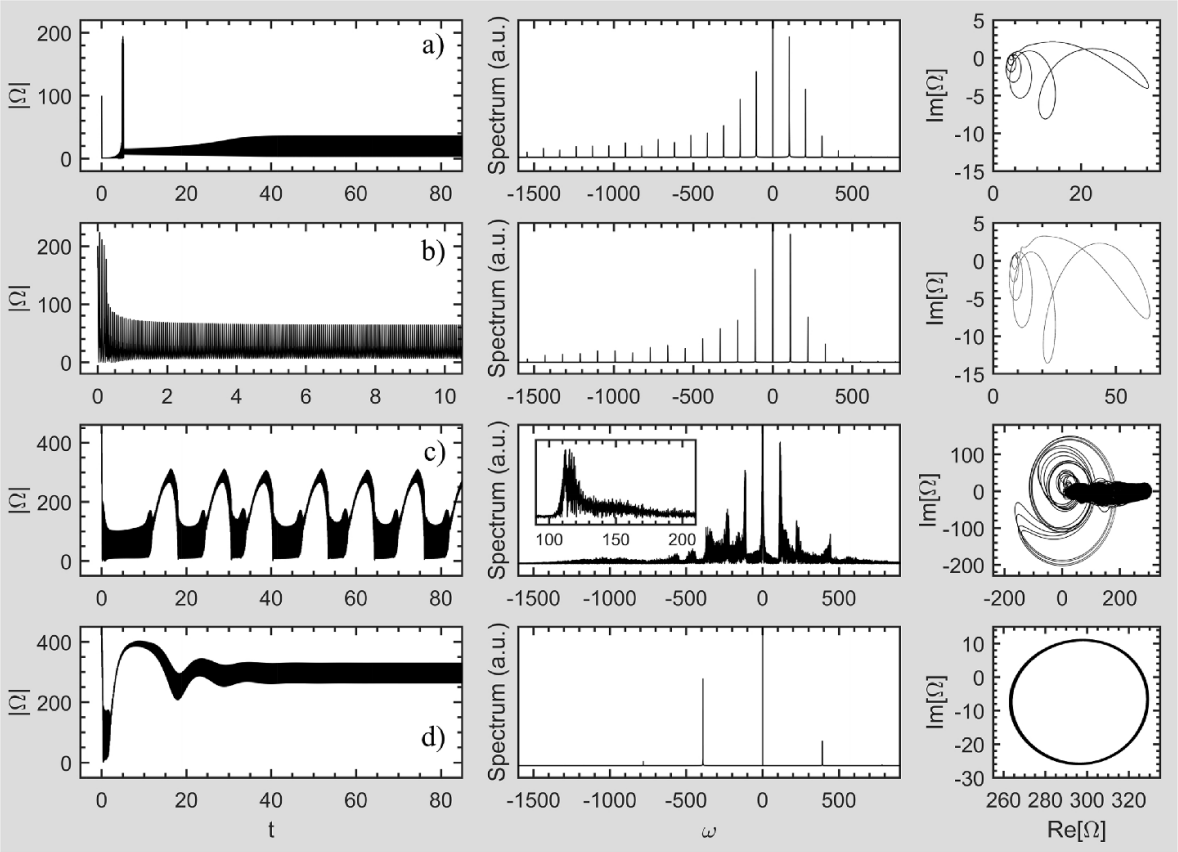

Figure 6. Time-domain behavior of the Rabi magnitude $|\Omega(t)|$ of the mean field (left column), the Fourier magnitude spectrum $\bar{f}(\omega)$ (central column), and the two-dimensional phase-space map $(\mathrm{Re}\,\Omega], \mathrm{Im}\,\Omega)$ of the attractor (right column) calculated for the ground state as the initial condition, the doublet splitting $\Delta_{21} = 100$, and the relaxation constant $\gamma_{21} = 0.01$. Three values of the Rabi magnitude $|\Omega_0|$ of the incident field were used in these calculations: upper row (a) $|\Omega_0| = 100$, row (b) $|\Omega_0| = 200$, row (c) $|\Omega_0| = 301.4$, and lower row (d) $|\Omega_0| = 400$. The inset blows up a continuous feature of the Fourier spectrum.

and is considered to be one of the possible ways to encode information [63].

Figure 6 shows the mean-field dynamics calculated for the doublet splitting $\Delta_{21} = 100$, the relaxation constant $\gamma_{21} = 0.01$, and the ground-state initial conditions. Three values of the Rabi magnitude $|\Omega_0|$ of the incident field were considered (these are indicated by arrows in lower left panel of figure 2): upper row (a) $|\Omega_0| = 100$, row (b) $|\Omega_0| = 200$, row (c) $|\Omega_0| = 301.4$, and lower row (d) $|\Omega_0| = 400$. The three columns show the time-domain behavior, the Fourier spectrum, and the phase map, respectively.

As can be seen from figure 6, for lower external field magnitudes, such as $|\Omega_0| = 100$ and $|\Omega_0| = 200$ the system evolves towards limit cycles, whereas for the larger $|\Omega_0| = 301.4$ the attractor is rather a chaotic orbit; the latter was also confirmed by the Lyapunov exponents analysis. As the external field is increased further, the system's attractor converts back to a simple limit cycle: see the case $|\Omega_0| = 400$ in figure 6. Bifurcations corresponding to these changes of the attractors can be clearly seen in figure 4 (they have been discussed above). In these four cases there is only one attractor for each value of $|\Omega_0|$ and therefore the system evolves towards it for whatever initial condition.

3.4. Qualitative reasoning

As was shown above, the monolayer optical response manifests a variety of fascinating properties: hysteresis, self-oscillations, and chaos. The physical origin of these effects is the secondary field acting on an emitter; the latter field depends on the current state of the emitter itself resulting in a nonlinear feedback which gives rise to various instabilities.

To demonstrate our reasoning, we consider equations (5*d*) and (5*e*). Substituting therein the expression (2) for the mean-field Rabi amplitude Ω, one obtains

$$\begin{aligned}\dot{\rho}_{31} = &-[i\Delta_{31} + \Gamma_{31} \\ &- (\gamma_{\mathrm{R}} - i\Delta_{\mathrm{L}})(Z_{31} - \mu\rho_{21})]\,\rho_{31} \\ &+ \mu(\gamma_{\mathrm{R}} - i\Delta_{\mathrm{L}})(Z_{31} - \mu\rho_{21})\rho_{32} \\ &+ \Omega_0(Z_{31} - \mu\rho_{21}),\end{aligned} \tag{6a}$$

$$\begin{aligned}\dot{\rho}_{32} = &-[i\Delta_{32} + \Gamma_{32} \\ &- \mu(\gamma_{\mathrm{R}} - i\Delta_{\mathrm{L}})(\mu Z_{32} - \rho_{21}^{*})]\,\rho_{32} \\ &+ (\gamma_{\mathrm{R}} - i\Delta_{\mathrm{L}})(\mu Z_{32} - \rho_{21}^{*})\rho_{31} \\ &+ \Omega_0(\mu Z_{32} - \rho_{21}^{*}),\end{aligned} \tag{6b}$$

where $\Gamma_{31} = \frac{1}{2}(\gamma_{31} + \gamma_{32})$, $\Gamma_{32} = \frac{1}{2}(\gamma_{31} + \gamma_{32} + \gamma_{21})$, $Z_{31} = \rho_{33} - \rho_{11}$, and $Z_{32} = \rho_{33} - \rho_{22}$. Equations (6*a*) and (6*b*) describe two coupled nonlinear oscillators driven by external forces. An important peculiarity of this system is that all oscillator characteristics, such as frequencies, relaxation rates, coupling strengths, and the driving force amplitudes depend on the current state of the Λ-emitter. These dependencies originate from the secondary field (produced by all other emitters) which acts on the given emitter. Note that such field is absent in equations for an isolated emitter. The secondary field results in (a) the renormalization of the transition frequencies, that is $\omega_{31} \to \omega_{31} + \Delta_L Z_{31} + \mu\,\mathrm{Im}[(\gamma_R - i\Delta_L)\rho_{21}]$ and $\omega_{32} \to \omega_{32} + \mu^2\Delta_L Z_{21} + \mu\,\mathrm{Im}[(\gamma_R - i\Delta_L)\rho_{21}^*]$ for transitions $1 \leftrightarrow 3$ and $2 \leftrightarrow 3$, respectively, and (b) in the additional damping of the two transitions described by $-\gamma_R Z_{31} + \mu\,\mathrm{Re}[(\gamma_R - i\Delta_L)\rho_{21}]$ and $-\mu^2\gamma_R Z_{32} + \mu\,\mathrm{Re}[(\gamma_R - i\Delta_L)\rho_{21}^*]$. As can be seen, both renormalizations depend on the current state of the considered emitter itself, thus having a *dynamic* nature.

In the absence of the incident field the states $|2\rangle$ and $|3\rangle$ are not populated, for which reason $Z_{32}(0) = 0$ and $\rho_{21}(0) = 0$ whereas $Z_{31}(0) = -1$ and, therefore, only the transition $1 \leftrightarrow 3$ experiences the above mentioned renormalization. The initial conditions in this case are the following: the actual detuning from the $1 \leftrightarrow 3$ resonance is $(\Delta_{31} - \Delta_L)$ while the initial relaxation rate of this transition is $(\gamma_{31} + \gamma_{32})/2 + \gamma_R$. Given that $\Delta_L \gg \Delta_{31}$ and $\gamma_R \gg (\gamma_{31} + \gamma_{32})/2$, it is Δ_L and γ_R that determine the resonance detuning and the relaxation rate of the $1 \leftrightarrow 3$ transition initially. All other resonance detunings and decay rates remain unchanged.

The second terms in the right-hand sides of equations (6*a*) and (6*b*) couple the two oscillators through the secondary field: ρ_{31} is coupled to ρ_{32} with the strength $(\gamma_R - i\Delta_L)(Z_{31} - \mu\rho_{21})$ while ρ_{32} is coupled to ρ_{31} with the strength $(\gamma_R - i\Delta_L)(\mu Z_{32} - \rho_{21}^*)$. Initially, the oscillators are decoupled because $Z_{32}(0) = \rho_{32}(0) = \rho_{21}(0) = 0$. However, they start coupling to each other as soon as the upper doublet state $|2\rangle$ is populated, which occurs immediately after the population of the upper state $|3\rangle$ and subsequent decay to the state $|2\rangle$ of the doublet. Such coupling of the transitions $2 \leftrightarrow 1$ and $3 \leftrightarrow 2$ results in an additional *dynamic* coupling-driven renormalization of the transition frequencies and relaxation rates. In what follows, we will refer to the whole secondary-field-driven renormalization of Λ-emitter's states/transitions as to dressing.

We believe that a complicated interplay of the above mentioned dynamic dressing effects, which change the resonance conditions and redistribute population among levels, gives rise finally to various instabilities of the system's response.

4. Reflectance

In our analysis of the monolayer optical response we used the Rabi amplitude Ω of the mean field as the studied output. In experiment, however, the reflected or transmitted field intensity is commonly measured. These two fields are determined by the far-zone part of Ω and are given by the following expressions:

$$\Omega_{\mathrm{refl}} = \gamma_R(\rho_{31} + \mu\rho_{32})\,. \tag{7a}$$

$$\Omega_{\mathrm{tr}} = \Omega_0 + \gamma_R(\rho_{31} + \mu\rho_{32})\,. \tag{7b}$$

The reflectance R and transmittance T (reflection and transmission coefficients of the light flow, respectively) are then defined as

$$R = \left|\frac{\Omega_{\mathrm{refl}}}{\Omega_0}\right|^2, \quad T = \left|\frac{\Omega_{\mathrm{tr}}}{\Omega_0}\right|^2. \tag{8}$$

4.1. Stationary reflectance

First, we address the linear regime of excitation ($|\Omega_0| \ll 1$) and restrict ourselves to the analysis of the steady-state reflectance (hereafter we use the term steady-state referring to a state with a constant amplitude in the RWA). Under this condition and at $|\Omega_0| \ll 1$, the major contribution to Ω_{refl} comes from ρ_{31} which is given by

$$\rho_{31} = -\frac{\Omega_0}{i(\Delta_{31} - \Delta_L) + \frac{1}{2}(\gamma_{31} + \gamma_{32}) + \gamma_R}\,. \tag{9}$$

Substituting equation (9) into equation (8), for the reflectance R we get

$$R = \frac{\gamma_R^2}{(\Delta_{31} - \Delta_L)^2 + \left[\frac{1}{2}(\gamma_{31} + \gamma_{32}) + \gamma_R\right]^2}\,. \tag{10}$$

From this expression, it follows that for the range of detuning $\Delta_{31} \leqslant 100$ used in our calculations so far, the reflectance $R \approx (\gamma_R/\Delta_L)^2 \ll 1$, because $\Delta_L \gg \Delta_{31}, \gamma_R, \gamma_{31} + \gamma_{32}$ for the chosen parameter set. Note that all features of the mean field Ω, predicted in section 3, will also manifest themselves in the reflected field Ω_{refl} and thus they can be observed in the reflection geometry despite the fact that the reflectance is low.

On the other hand, in the vicinity of the resonance renormalized by the near field ($\Delta_{31} \sim \Delta_L$), the reflectance is close to unity, $R \approx 1$. Therefore, in this range of frequencies, the monolayer of Λ-emitters can operate as an almost perfect reflector. Similar behaviour has been reported recently for a monolayer of $MoSe_2$ [5, 6] and arrays of atoms trapped in optical lattices [64].

Next, we analyze the steady-state reflection in the nonlinear regime in the vicinity of the detuning $\Delta_{31} \sim \Delta_L$, where the linear reflectance is high. Figure 7 shows the intensity-dependent reflectance calculated for two values of the relaxation rate: $\gamma_{21} = 0.01$ (left column) and $\gamma_{21} = 0.05$ (right column), and two values of the doublet splitting: $\Delta_{21} = 15$ (upper panels) and $\Delta_{21} = 100$ (lower panels). Stable branches of these dependencies are given by solid black lines, while the unstable ones by dashed ones. The figure shows that the reflectance is non-monotonous, it can be multivalued and unstable for different detunings Δ_{31} (specified in each panel). For the vast majority of the considered parameter sets, the reflectance is unstable in a very wide range of incident field intensities: see, for example, the curve for $\Delta_{31} = 1000$ in the upper-left panel; it is striking also that the reflectance is unstable at

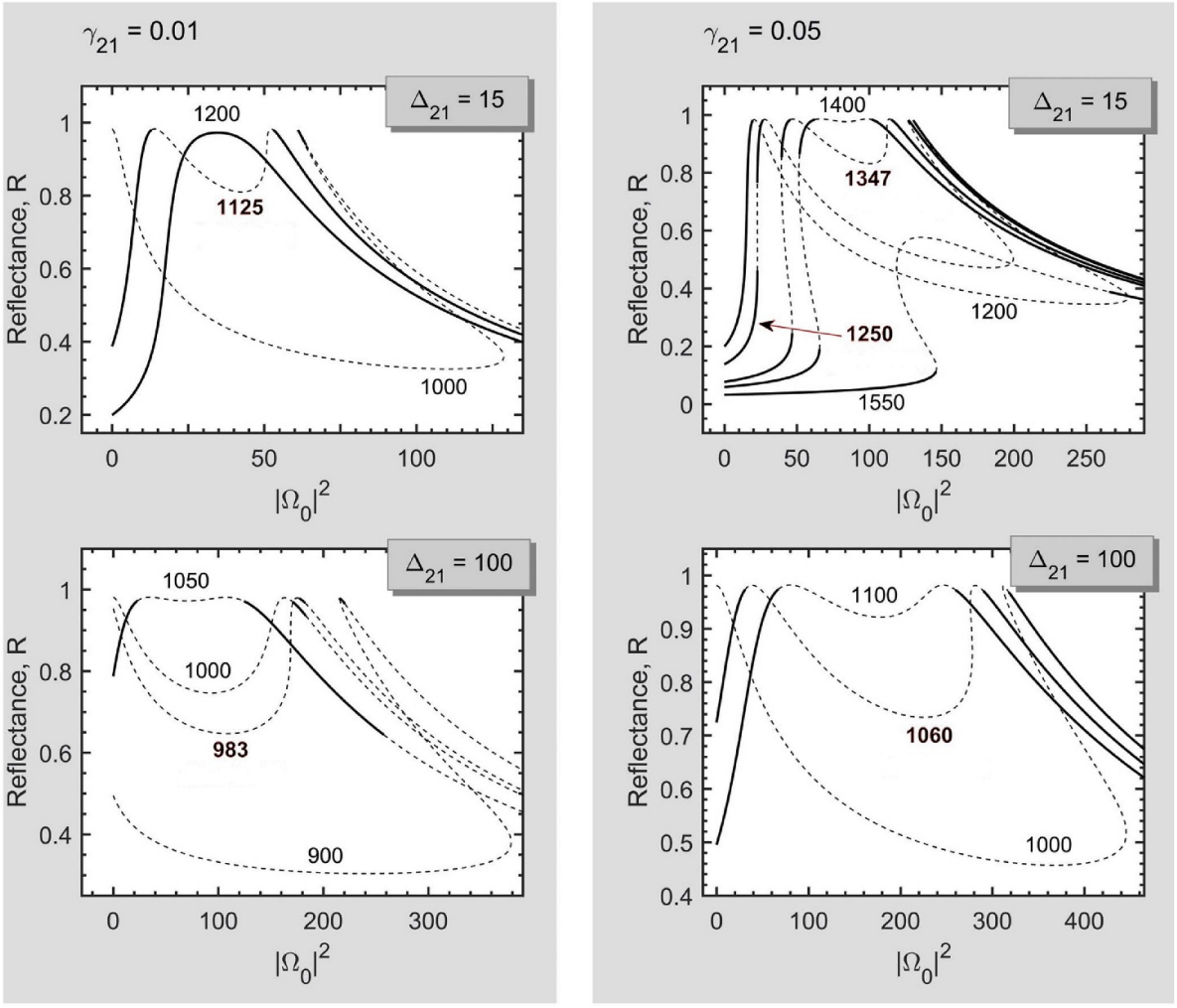

Figure 7. Intensity dependence of the stationary reflectance R calculated for detunings Δ_{31} in the vicinity of $\Delta_{31} = \Delta_L$ for two values of the relaxation rate $\gamma_{21} = 0.01$ (left plot) and $\gamma_{21} = 0.05$ (right plot) and two values of the doublet splitting $\Delta_{21} = 15$ (upper panels) and $\Delta_{21} = 100$ (lower panels). The values of Δ_{31} are specified next to the corresponding curves. Stable (unstable) branches of the reflectance are shown by solid (dashed) lines. The arrow indicates the threshold case in which the reflectance becomes bistable.

very low external field intensities, which manifests itself in its auto-oscillations (see below). Another unusual feature of the nonlinear reflectance is that it is double-peaked for some parameter sets. Surprisingly, the reflection at these peaks is close to the total one, $R \approx 1$. The double-peak structure of the reflectance suggests that the system is driven into resonance with the incident field twice as the intensity of the latter is changed. Below we provide an explanation of such a behaviour.

Despite the fact that the system is now in a strongly nonlinear regime, the problem can be partially handled analytically in the following way. Consider equations (6*a*) and (6*b*) in the stationary regime: $\dot{\rho}_{31}(t) = \dot{\rho}_{32}(t) = 0$. Solving them formally for the variables ρ_{31} and ρ_{32}, we can derive the quantity $\rho_{31} + \mu\rho_{32}$ which determines the Rabi amplitude of the reflected field Ω_{refl} and obtain the reflectance R:

$$R = \left| \frac{\gamma_R \bar{\rho}}{(i\Delta_{31} + \Gamma_{31})(i\Delta_{32} + \Gamma_{32}) - (\gamma_R - i\Delta_L)\bar{\rho}} \right|^2, \tag{11}$$

$$\bar{\rho} = \mu(i\Delta_{31} + \Gamma_{31})(\mu Z_{32} - \rho_{21}^*) + (i\Delta_{32} + \Gamma_{32})(Z_{31} - \mu\rho_{21}) .$$

The denominator D of the fraction in this expression is a quadratic function in Δ_{31} (recall that $\Delta_{32} = \Delta_{31} - \Delta_{21}$) and can therefore be written as $D = (\Delta_{31} - \Delta_+)(\Delta_{31} - \Delta_-)$. The latter suggests that the peaks in reflection are related to the complex-valued poles $\Delta_\pm$ of the fraction, *i.e.*, with the complex-valued zeroes of the denominator D. The real parts of the poles $\Delta_\pm$ determine peak positions, while the imaginary parts—peak widths. As the poles $\Delta_\pm$ depend on the density matrix elements, they are obtained after solving the whole nonlinear stationary problem.

The physical meaning of the poles $\Delta_\pm$ can be understood bearing in mind that the denominator D in equation (11) is also the determinant of the system of equations (6*a*) and (6*b*) in the stationary regime. Therefore, the zeros $\Delta_\pm$ determine the 'eigen detunings' (or eigen frequencies) of the two dressed Λ-emitter steady states. Thus, the two peaks of the steady-state reflectance emerge when the incident field is in resonance with one or the other dressed Λ-emitter transitions.

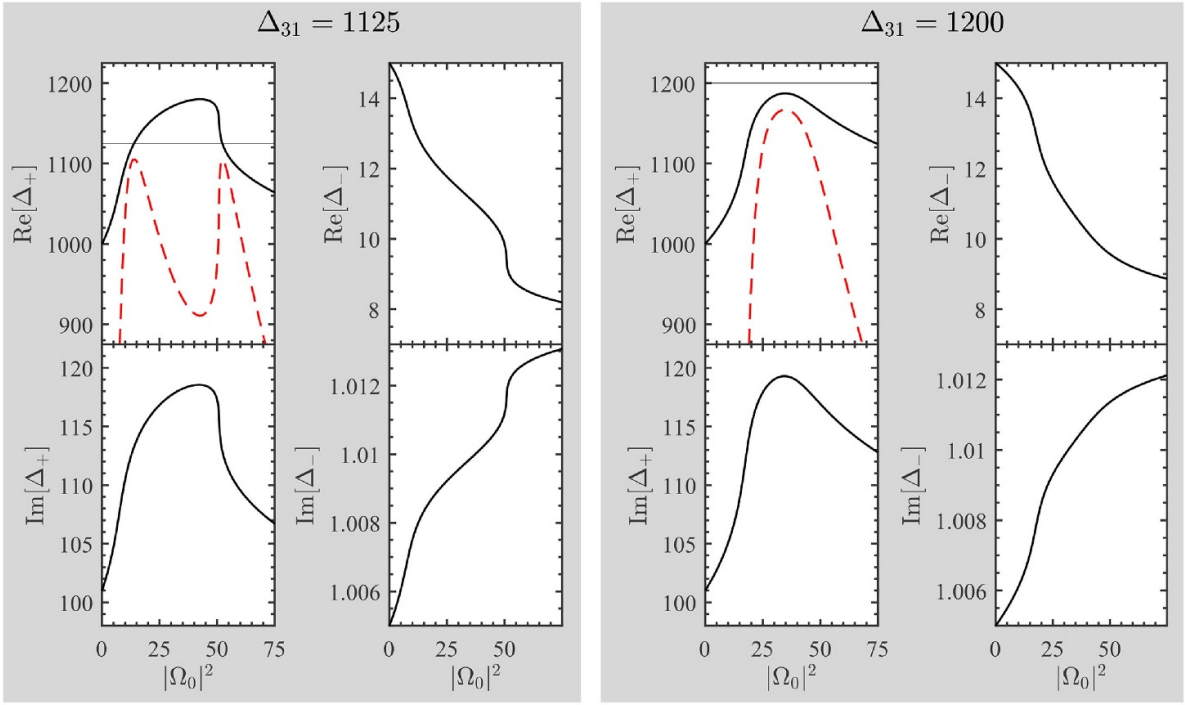

Figure 8. Intensity dependence of the poles $\Delta_\pm$ of equation (11) (solid curves) calculated for $\Delta_{31} = 1125$ (left plot) and $\Delta_{31} = 1200$ (right plot). Dashed curves show the rescaled reflectance ($\Delta_{31}R$) which is given for reference; horizontal thin lines denote the level Δ_{31} which correspond to the unity rescaled reflectance. Parameters of the doublet are: $\Delta_{21} = 15$, $\gamma_{21} = 0.01$. Other parameters are specified in the text.

Figure 8 shows the intensity dependencies of the poles $\Delta_\pm$ (solid curves) calculated for the doublet splitting $\Delta_{21} = 15$, relaxation rate $\gamma_{21} = 0.01$, and two values of the incident field detunings: $\Delta_{31} = 1125$ (left plot) and $\Delta_{31} = 1200$ (right plot). The corresponding dependencies of the reflectance (scaled by Δ_{31}) are shown by dashed lines. Thin horizontal grid lines indicate the value Δ_{31}. It becomes clear from the plots that peaks in the reflectance occur when the real part of the pole crosses the grid line: $\mathrm{Re}\,\Delta_+ = \Delta_{31}$, i.e. when a dressed state is in resonance with the incident field. At $\Delta_{31} = 1125$, there are two such intersections giving rise to two peaks of the reflectance R. The fact that the peak value of R is close to unity (almost total reflection) can be explained by the resonant nature of the excitation in which case the incident and the secondary fields are almost equal in magnitude, but opposite in phase; they interfere destructively resulting in almost zero transmitted field and almost total reflection.

In the case of $\Delta_{31} = 1200$ (see the right panel in figure 8), there is no intersection of the curve $\mathrm{Re}\,\Delta_+$ with the grid line at Δ_{31}. However, the curve approaches close enough to the line, which gives rise to one single strong peak in the reflectance. Because $\mathrm{Re}\,\Delta_+$ is never equal to Δ_{31}, the system is never in exact resonance and therefore the incident and the secondary fields are compensating each other to a lesser extent. Consequently, the peak value of R is somewhat smaller than in the resonant case. The reflectance in the vicinity of the second root Δ_- is not shown here because it is low.

The double-peak structure of the reflectance is a unique feature of the systems which differs it from other three-level systems such as the ladder-like one [29]. Finally, we note that figure 7 shows that the stationary reflectance can be unstable even for very low incident field intensities for some parameter sets. This suggests that 2D systems of Λ-emitters can manifest nonlinear behavior under low excitation conditions, which can be an advantage for applications; it also makes such systems very different from may other nonlinear ones. In the next section we explore this peculiar behaviour in the time domain.

4.2. Reflectance dynamics

As we showed in the previous section, the reflectance R can be unstable within some range of the incident field intensities $|\Omega_0|^2$. Surprisingly, instabilities can appear at relatively low values of intensity $|\Omega_0|^2 \lesssim 1$ (see, for example, the upper left panel of figure 7). To uncover the character of these instabilities, we performed time-domain calculations of the reflectance R within the unstable region for different sets of parameters and $|\Omega_0|^2 = 1$. The results are presented in figure 9 which shows that in all considered cases the system manifests periodic self-oscillations. The latter can be understood from the equidistant character of the peaks in the Fourier magnitude spectrum $\bar{f}_{\mathrm{refl}}(\omega) = |\int_T \Omega_{\mathrm{refl}}(t)\, e^{i\omega t} dt|$ (see plots in the middle column) and the fact that the trajectory is closed in the phase-space ($\mathrm{Re}\,\Omega_{\mathrm{refl}}$, $\mathrm{Im}\,\Omega_{\mathrm{refl}}$) (see the panels in the right column). We have not found other types of attractors in the case of moderate intensities, $|\Omega_0|^2 \sim 1$.

Note that the Fourier spectrum of self-oscillations contains harmonics in the THz domain (see panels *b* and *d* of figure 9). Thus, the system can operate as a source of coherent THz radiation.

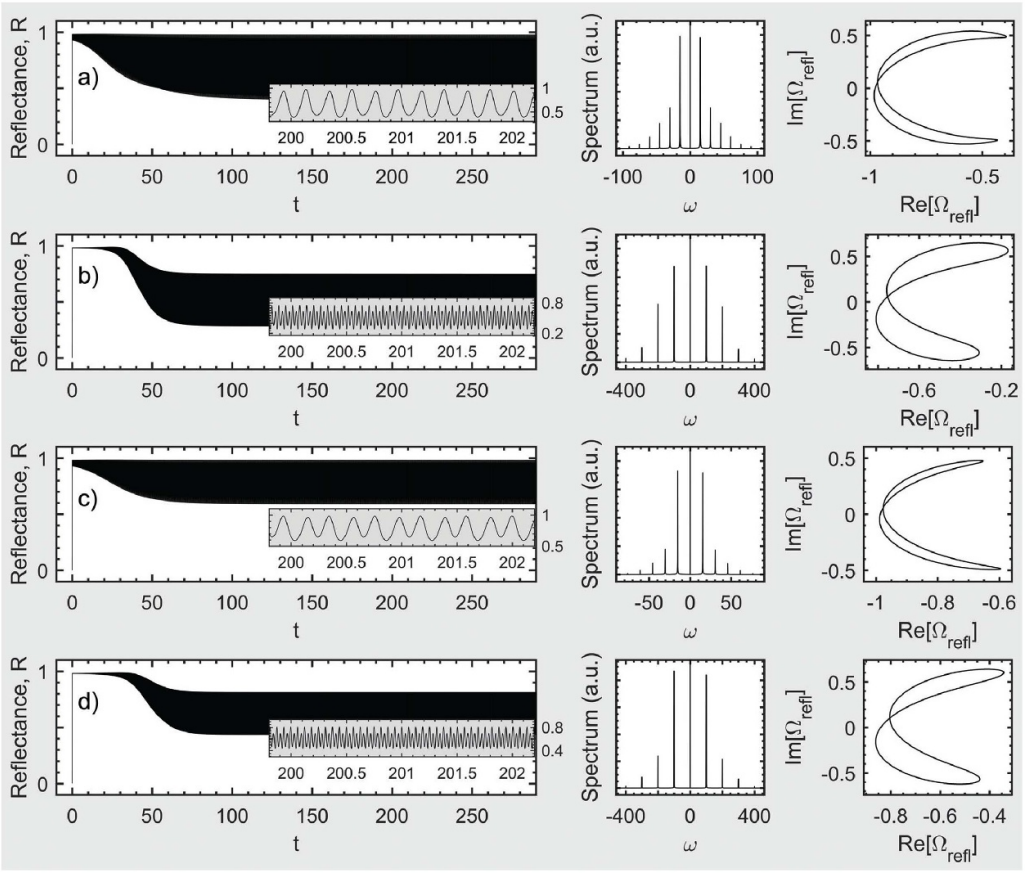

Figure 9. Time-domain behavior of the reflectance R (left column), the Fourier magnitude spectrum $\bar{f}_{\mathrm{refl}}(\omega)$ (middle column) and the two-dimensional phase-space map ($\mathrm{Re}\,\Omega_{\mathrm{refl}}$, $\mathrm{Im}\,\Omega_{\mathrm{refl}}$) of the attractor (right column) obtained by solving equations (5*a*)–(5*f*) for the detuning $\Delta_{31} = 1000$ with the ground-state initial condition, and Rabi magnitude of the incident field $|\Omega_0| = 1$. Other parameters are: (a) $\Delta_{21} = 15$, $\gamma_{21} = 0.01$; (b) $\Delta_{21} = 100$, $\gamma_{21} = 0.01$; (c) $\Delta_{21} = 15$, $\gamma_{21} = 0.05$; (d) $\Delta_{21} = 100$, $\gamma_{21} = 0.05$. The insets blow up the dynamics.

5. Summary

We have studied theoretically the optical response of a quantum metasurface comprising regular array of Λ-emitters subjected to a CW quasi-resonant excitation. The total field, driving the optical transitions of an emitter, has been taken into account within the framework of the mean-field approximation; this field depends on the current state of the emitter itself and introduces a feedback into the system, giving rise to various nonlinear effects.

First, we have addressed the stationary optical response and analyzed its stability using the local Lyapunov exponents. We have shown that the optical response can be multi-valued and unstable within a wide range of parameters. We have demonstrated also that under some conditions the unstable state is the only possible state of the system, which makes it very different from other 2D nonlinear systems. Second, we have calculated the bifurcation diagram for the system in order to get a general insight into possible kinds of the system optical dynamics. Different types of bifurcations, such as supercritical and subcritical Andronov-Hopf ones, limit cycle folding points, and limit cycle–chaos bifurcations have been found. Bifurcation diagrams show also that instabilities can emerge even at very low incident field intensities, which is an important advantage of the considered system from the point of view of practical applications. We argue that the unstable dynamics originates from the complicated interplay of the secondary field–driven dynamic dressing of the emitter's transitions and dynamic population redistribution among the dressed states.

Remarkably, for frequencies in the vicinity of the collective (excitonic) resonance, the monolayer reflects the incident field almost completely, operating as a perfect mirror. Unlike other nanoscale 2D systems with similar properties, the reflectance of the metasurface of Λ-emitters can have two almost unity peaks, which is a unique feature that can be useful for applications. Besides, the reflectance can manifest bistability and hysteresis: it can therefore be switched abruptly between low and high state back and forth by small variations of the incident field intensity.

Using the time domain calculations, we have demonstrated that the monolayer optical response can have very different types of dynamics under a CW excitation, ranging from various periodic self-oscillations to chaotic behavior. We have shown also that the frequency of the self-oscillations depends on the incident field magnitude and, for some sets of parameters, falls in the THz domain.

Our results suggest various practical applications of metasurfaces of quauntum Λ-emitters, such as a nanometer-size bistable mirror, a tunable generator of coherent THz radiation (in the self-oscillation regime), or an optical noise generator (in the chaotic regime). The intrinsic sensitivity of the optical response to the initial conditions in the chaotic regime could be of interest for the information encryption [63]. The proposed metasurface could be taken as yet another example of a nanoscale 2D system with remarkable optical properties. We showed, however, that unlike other systems a metasurface comprising Λ-emitters can manifest nonlinear properties at very low field intensities (on the order of 1 W/cm^2); this is a very unusual property which will be addressed in more detail elsewhere. Also, systems based on the SQDs as quantum emitters have an important advantage: their properties can be engineered by choosing the geometry, sizes, and materials of the underlying nanostructures. Moreover, we showed that the optical response of the system is very sensitive to the doublet splitting and relaxation, which can be tuned in an experiment, for example, by the magnetic field, the temperature, etc. The latter provides a possibility of the real-time control and tuning of the optical response, which makes the proposed systems particularly suitable for applications. All these findings make the considered system a promising candidate for the all-optical information processing and computing devices; they can also be a useful guide for new experiments.

Data availability statement

The data that support the findings of this study are available upon reasonable request from the authors.

Acknowledgments

R F M acknowledges M Akmullah Bashkir State Pedagogical University for a financial support. A V M acknowledges support from Spanish MICIN Grants MAT2016-75955 and PID2019-106820RB-C21.

ORCID iDs

Ramil F Malikov https://orcid.org/0000-0003-3457-0135
Andrey V Malyshev https://orcid.org/0000-0002-6011-6975

References

[1] Novoselov K S, Geim A K, Morozov S V, Jiang D, Zhang Y, Dubonos S V, Grigorieva I V and Firsov A A 2004 *Science* **306** 666
[2] Neto A H C, Guinea F, Peres N M R, Novoselov K S and Geim A K 2009 *Rev. Mod. Phys.* **81** 109
[3] Manzeli S, Ovchinnikov D, Pasquier D, Yazyev O V and Kis A 2017 *Nat. Rev. Mater.* **2** 17033
[4] Chernozatonskii L A and Artyukh A A 2018 *Phys.-Usp.* **61** 2
[5] Back P, Zeytinoglu S, Ijaz A, Kroner M and Imamoğlu A 2018 *Phys. Rev. Lett.* **120** 037401
[6] Scuri G *et al* 2018 *Phys. Rev. Lett.* **120** 037402
[7] Bonaccorso F, Lombardo A, Hasan T, Sun Z, Colombo L and Ferrari A C 2012 *Mater. Today* **15** 564
[8] Bhimanapati G R *et al* 2015 *ACS Nano* **9** 11509
[9] Tan C *et al* 2017 *Chem. Rev.* **117** 6225
[10] Solntsev A S, Agarwal G S and Kivshar Y S 2021 *Nat. Photon.* **15** 327–36
[11] Jariwala D, Marks T J and Hersam M C 2017 *Nat. Mater.* **16** 170
[12] Evers W H, Goris B, Bals S, Casavola M, de Graaf J, van Roij R, Dijkstra M and Vanmaekelbergh D 2013 *Nano Lett.* **13** 2317
[13] Baranov A V, Ushakova E V, Golubkov V V, Litvin A P, Parfenov P S, Fedorov A V and Berwick K 2015 *Langmuir* **31** 506
[14] Ushakova E V, Cherevkov S A, Litvin A P, Parfenov P S, Volgina D O A, Kasatkin I A, Fedorov A V and Baranov A V 2016 *J. Phys. Chem.* C **120** 25061
[15] Liu W *et al* 2017 *Nat. Chem.* **9** 563
[16] Mu P, Zhou G and Chen C L 2018 *Nano-Struct. Nano-Objects* **15** 153
[17] Bettles R J, Gardiner S A and Adams C S 2016 *Phys. Rev. Lett.* **116** 103602
[18] Facchinetti G and Ruostekoski J 2018 *Phys. Rev.* A **97** 023833
[19] Williamson L A, Borgh M O and Ruostekoski J 2020 *Phys. Rev. Lett.* **125** 073602
[20] Baimuratov A S, Rukhlenko I D, Turkov V K, Baranov A V and Fedorov A V 2013 *Sci. Rep.* **3** 1727
[21] Baimuratov A S, Rukhlenko I D and Fedorov A V 2013 *Opt. Lett.* **38** 2259
[22] Baimuratov A S, Shlykov A I, Zhu W, Leonov M Y, Baranov A V, Fedorov A V and Rukhlenko I D 2017 *Opt. Lett.* **42** 2423
[23] Perczel J, Borregaard J, Chang D E, Pichler H, Yelin S F, Zoller P and Lukin M D 2017 *Phys. Rev.* A **96** 063801
[24] Vovk I A, Tepliakov N V, Baimuratov A S, Leonov M Y, Baranov A V, Fedorov A V and Rukhlenko I D 2018 *Phys. Chem. Chem. Phys.* **20** 25023
[25] Nossa J F and Camacho A S 2008 *Microelectron. J.* **39** 1251
[26] Baimuratov A S, Gun'ko Y K, Baranov A V, Fedorov A V and Rukhlenko I D 2016 *Sci. Rep.* **6** 23321
[27] Malikov R F, Ryzhov I V and Malyshev V A 2017 *EPJ Web Conf.* **161** 02014
[28] Malyshev V A, Zapatero P A, Malyshev A V, Malikov R F and Ryzhov I V 2019 *J. Phys.: Conf. Ser.* **1220** 012006
[29] Ryzhov I V, Malikov R F, Malyshev A V and Malyshev V A 2019 *Phys. Rev.* A **100** 033820
[30] Vlasov R A, Lemeza A M and Gladush M G 2013 *J. Appl. Spectrosc.* **80** 698
[31] Vlasov R A, Lemeza A M and Gladush M G 2013 *Laser Phys. Lett.* **10** 045401
[32] Bayramdurdiyev D, Malikov R, Ryzhov I and Malyshev V 2019 *EPJ Web Conf.* **220** 03004
[33] Bayramdurdiyev D Y, Malikov R F, Ryzhov I V and Malyshev V A 2020 *J. Exp. Theor. Phys.* **131** 244
[34] Brunner D, Gerardot B D, Dalgarno P A, Wüst G, Karrai K, Stoltz N G, Petroff P M and Warburton R J 2009 *Science* **325** 70
[35] Baba K, Kasai H, Nishida K and Nakanishi H 2011 *Functional Organic Nanocrystals* (London: IntechOpen) ch 15, p 397
[36] Benedict M G, Zaitsev A I, Malyshev V A and Trifonov E D 1990 *Opt. Spectrosc.* **68** 473
[37] Benedict M G, Zaitsev A I, Malyshev V A and Trifonov E D 1991 *Phys. Rev.* A **43** 3845
[38] Ben-Aryeh Y, Bowden C M and Englund J C 1986 *Phys. Rev.* A **34** 3917
[39] Basharov A M 1988 *Sov. Phys. - JETP* **67** 1741
[40] Oraevsky A N, Jones D J and Bandy D K 1994 *Opt. Commun.* **111** 163

[41] Malyshev V A and Jarque E C 2000 *Opt. Express* **6** 227
[42] Glaeske H, Malyshev V A and Feller K H 2000 *J. Chem. Phys.* **113** 1170
[43] Klugkist J A, Malyshev V A and Knoester J 2007 *J. Chem. Phys.* **127** 164705
[44] Malikov R F and Malyshev V A 2017 *Opt. Spectrosc.* **122** 955
[45] Andronov A A, Vitt A A and Khaikin S E 1966 *Theory Of Oscillators* (New York: Pergamon)
[46] Eckmann J P and Ruelle D 1985 *Rev. Mod. Phys.* **57** 617
[47] Guckenheimer J and Holmes P 1986 *Nonlinear Oscillations and Dynamical Systems and Bifurcations of Vector Fields* (Berlin: Springer)
[48] Neimark Y I and Landa P S 1992 *Stochastic and Chaotic Oscillations* (Berlin: Springer Science & Bussiness Media) (https://doi.org/10.1007/978-94-011-2596-3)
[49] Ott E 1993 *Chaos in Dynamical Systems* (Cambridge: Cambridge University Press)
[50] Arnold V I, Afrajmovich V S, Il'yashenko Y S and Shil'nikov L P 1994 *Dynamical Systems V: Bifurcation Theory and Catastrophe Theory* (Berlin: Springer)
[51] Alligood K T, Sauer T D and Yorke J A 1996 *Chaos: An Introduction to Dynamical Systems* (Berlin: Springer)
[52] Katok A and Hasselblatt B 1997 *Introduction to the Modern Theory of Dynamical Systems* (Cambridge: Cambridge University Press)
[53] Kuznetsov Y A 2004 *Elements of Applied Bifurcation Theory* 3rd edn (Berlin: Springer)
[54] Ryzhov I, Malikov R, Malyshev A and Malyshev V 2019 *EPJ Web Conf.* **220** 02012
[55] Lindblad G 1976 *Commun. Math. Phys.* **48** 119
[56] Blum K 2012 *Density Matrix: Theory and Applications* 3rd edn (Berlin: Springer)
[57] Born M and Wolf E 1980 *Principles of Optics* 6th edn (Berlin: Springer)
[58] Dicke R H 1954 *Phys. Rev.* **93** 99
[59] Trifonov E D, Zaitsev A I and Malikov R F 1979 *Sov. Phys. - JETP* **49** 33
[60] Benedict M G, Ermolaev A M, Malyshev V A, Sokolov I V and Trifonov E D 1996 *Super-Radiance: Multiatomic Coherent Emission* (Bristol: IOP Publishing)
[61] Lai Y C and Tél T 2011 *Transient Chaos. Complex Dynamics in Finite-Time Scales* (Berlin: Springer)
[62] Tél T 2015 *Chaos* **25** 097619
[63] Gao T and Chen Z 2008 *Phys. Lett.* A **372** 394
[64] Bekenstein R, Pikovski I, Pichler H, Shahmoon E, Yelin S F and Lukin M D 2020 *Nat. Phys.* **16** 676